PHYSICAL REVIEW B **101**, 195432 (2020)

# Landau level phases in bilayer graphene under pressure at charge neutrality

Brett R. Green [1,*] and Jorge O. Sofo [1,2,3,†]
[1] *Department of Physics, The Pennsylvania State University, University Park, Pennsylvania 16802, USA*
[2] *Department of Materials Science and Engineering, The Pennsylvania State University, University Park, Pennsylvania 16802, USA*
[3] *Materials Research Institute, The Pennsylvania State University, University Park, Pennsylvania 16802, USA*

(Received 10 February 2020; revised manuscript received 1 April 2020; accepted 28 April 2020; published 21 May 2020)

Bilayer graphene in a magnetic field hosts a variety of ordered phases built from eight Landau levels close in energy to the neutrality point. These levels are characterized by orbital $n = 0, 1$, valley $\xi = +, -$, and spin $\sigma = \uparrow, \downarrow$; their relative energies depend strongly on the Coulomb interaction, magnetic field, and interlayer bias. We treat interactions at the Hartree-Fock level, including the effects of metallic gates, layer separation, spatial extent of the $p_z$ orbitals, all Slonczewski-Weiss-McClure tight-binding parameters, and pressure. We obtain the ground state as function of the applied magnetic field, bias, and pressure. The gates, layer separation, and extent of the $p_z$ orbitals weaken the Coulomb interaction at different length scales; these effects distort the phase diagram but do not change its topology. However, previously predicted continuous transitions become discontinuous when all tight-binding parameters are included nonperturbatively. We find that pressure increases the importance of the noninteracting scale with respect to the Coulomb energy, which drives phase transitions to occur at lower fields. This brings two orbitally polarized states not yet predicted or observed into the experimentally accessible region of the phase diagram, in addition to previously identified valley-polarized, spin-polarized, and partially orbitally polarized states.

DOI: 10.1103/PhysRevB.101.195432

## I. INTRODUCTION

Electrons in a magnetic field occupy highly degenerate states known as Landau levels (LLs). In multilayer two-dimensional (2D) materials, a perpendicular electric field can change the relative position in energy of electronic states near the Fermi level, offering an exciting platform for the exploration of quantum order in condensed matter systems. Bilayer graphene (BLG) is no exception, and it has been shown experimentally [1–5] to produce different macroscopic states, such as a fully spin-polarized state, a fully valley-polarized state, and others to be described below. The appearance of these states as a function of applied fields generates a phase diagram, which is a target of research in this area and provides a map for the study of these phases. Of course, the experimental identification of each ground state is challenging, and this work needs to be complemented by theoretical understanding of the system.

Recent experiments [1,2,4] on undoped (filling factor $\nu = 0$) BLG found a single sharp transition as the electric field was increased while the magnetic field was low, but at higher magnetic fields, the phase boundary splits into two. These transitions were identified by peaks in the sample's two-terminal conductivity. One low-field state is a fully spin-polarized or ferromagnetic state evolving from a canted antiferromagnetic state, identified by edge-state conductivity measurements [3,6,7]. The other two have been characterized by layer polarization measurements [1], which support the identification of the low-magnetic-field, high-electric-field state as a fully valley-polarized state, and of the intermediate state as one with mixed polarization in both spin and valley. The intermediate state is also the first to be observed with polarization in the orbital index $n$, an additional low-energy degree of freedom in BLG deriving from its unique LL spectrum: $E_0 \approx 0$, $E_1 \approx 0$, $E_{\pm n} \approx \pm\hbar\omega\sqrt{n(n-1)}$ for $n \geqslant 2$ [8].

The $\nu = 0$ phase diagram has proven to be highly sensitive to experimental perturbations, such as screening by an atomically thin dielectric [4] or changes in device geometry and size [3], underlining the possibilities for quantum state engineering and the importance of a careful treatment of interactions. In this work, we add a different method of manipulating states: pressure. We show that pressure can be used to control the orbital degree of freedom, and that this is achieved by changing the energy scale of the noninteracting dynamics relative to the interaction energy scale.

Regarding the treatment of interactions, two approaches have been used in previous work: one based on the bare Coulomb potential [9–13], and the other using only short-range interactions which may break symmetries of the bare Coulomb potential, an approach introduced by Kharitonov [6,14,15]. Additionally, Hunt *et al.* [1] treat the direct Coulomb interaction with a random phase approximation including metallic gates in the bare propagator in addition to symmetry-breaking parameters. On one hand, the former approach has no free parameters but has not yet reproduced the experimentally observed intermediate phase; on the other, the latter approach has succeeded in reproducing the intermediate phase but requires undetermined parameters whose physical

---

[*] brg5241@psu.edu

[†] sofo@psu.edu; http://sites.psu.edu/sofo

origins are not transparent. So that we can understand the underlying physics while exploring the effects of pressure, we take the parameter-free approach.

Previous use of this approach has included the effects of layer separation in Refs. [9–13] and screening by metallic gates in Ref. [1] when treating the interaction. We unify these by deriving a propagator which includes both effects, and also address the out-of-plane spatial extent of the $p_z$ orbitals with layer-resolved three-dimensional (3D) LL wave functions, which had previously been taken as 2D in each layer. These wave functions are derived by exact diagonalization of a four-band tight-binding Hamiltonian including all Slonczewski-Weiss-McClure tight-binding (TB) parameters, which we show are key in determining the nature (discontinuous, or continuously interpolating between ground states) of phase transitions. In particular, our model predicts a single sharp spin- to valley-polarized transition at low fields, which contrasts with the continuous transition mixing the states found in previous parameter-free studies [9–13]. Our results therefore impact the interpretation of this transition's experimental transport signature, which is not yet universally agreed upon.

Under pressure, we find two orbitally polarized states not yet predicted or observed. These states appear because pressure increases the energy gap between orbitals so that it overcomes the interaction energy scale, which stabilizes the spin- and valley-polarized states observed at low magnetic fields. Hence, pressure effectively tunes the strength of interactions relative to the noninteracting energy scale. Pressure can also be treated as a theoretical proxy in our results for other effects that influence the noninteracting energy scales.

The paper is outlined as follows. In Sec. II A, we solve the TB model in a magnetic field to find LL energies and wave functions. We then address interactions at the Hartree-Fock level in Sec. II B, and describe our approach to the interacting problem. Solving the interacting problem as a function of magnetic field and bias yields phase diagrams which we present in Sec. III. We also characterize the possible ground states in this section, and discuss how the effects we include in treatment affect our results. We summarize our work and findings, and suggest next steps, in Sec. IV.

## II. METHODS

### A. Noninteracting Hamiltonian

We begin with the spin-free TB Bloch Hamiltonian

$$H_{\boldsymbol{k}} = \begin{bmatrix} 2\varepsilon + \frac{\Delta}{2} & t\phi & t_4\phi^* & t_\perp \\ t\phi^* & \frac{\Delta}{2} & t_3\phi & t_4\phi^* \\ t_4\phi & t_3\phi^* & -\frac{\Delta}{2} & t\phi \\ t_\perp & t_4\phi & t\phi^* & 2\varepsilon - \frac{\Delta}{2} \end{bmatrix} \tag{1}$$

written in the basis $\{|A1,\boldsymbol{k}\rangle, |B1,\boldsymbol{k}\rangle, |A2,\boldsymbol{k}\rangle, |B2,\boldsymbol{k}\rangle\}$. Here, $|T\boldsymbol{k}\rangle = \frac{1}{\sqrt{N}}\sum_{\boldsymbol{R}} e^{i\boldsymbol{k}\cdot\boldsymbol{R}}|T\boldsymbol{R}\rangle$ is the Fourier transform of the $p_z$ orbitals $|T\boldsymbol{R}\rangle$ on the lattice site $T = T_{2D}T_z$ with sublattice $T_{2D} = A, B$ and layer $T_z = 1, 2$, located in the unit cell at $\boldsymbol{\tau}_T = \boldsymbol{\tau}_T^{2D} + \tau_T^z\hat{\boldsymbol{z}}$ with $\boldsymbol{\tau}_T^{2D}$ in the hexagonal lattice and layer $\tau_T^z = (-1)^{T_z+1}d/2$. $\boldsymbol{R}$ gives the location of the unit cell, and $N$ gives the number of unit cells in the sample. $t, t_\perp, t_3$, and $t_4$ are the hopping parameters, $\epsilon$ gives the site energy for stacked $A1$ and $B2$ atoms, and $\Delta$ is an interlayer bias induced by a perpendicular electric field. We follow the sign convention of Jung and MacDonald [16] for the TB parameters.

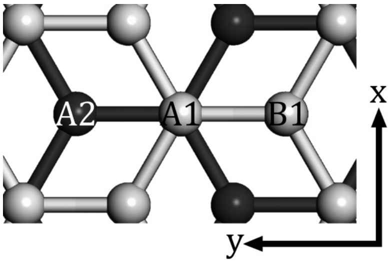

FIG. 1. The BLG unit cell has a four-atom basis with inequivalent $A$ and $B$ sites in each layer. They are shown here with upper layer sites are denoted as $A1$, $B1$ and lower layer sites as $A2$, $B2$. The $A1$ sites and $B2$ sites are stacked.

We expand $\phi = \phi(\boldsymbol{k})$ to linear order in $\boldsymbol{q} = \boldsymbol{k} - \boldsymbol{K}_\xi$ about valley $\xi$:

$$\phi(\boldsymbol{k}) = e^{ia_{CC}k_y}\left[1 + 2e^{-i\frac{3a_{CC}}{2}k_y}\cos\left(\frac{a_{CC}\sqrt{3}}{2}k_x\right)\right], \tag{2a}$$

$$\phi(\boldsymbol{K}_\xi + \boldsymbol{q}) \approx -\xi\frac{3a_{CC}}{2}(q_x - \xi iq_y) = -\xi\frac{3a_{CC}}{2}q_{-\xi}, \tag{2b}$$

where $a_{CC} = 0.142$ nm is the interatomic distance and $q_\pm = q_x \pm iq_y$. The lattice sites and coordinate system are depicted in Fig. 1.

We represent the magnetic field $\boldsymbol{B} = B\hat{\boldsymbol{z}}$ by a vector potential in the Landau gauge given by $\boldsymbol{A} = Bx\hat{\boldsymbol{y}}$. This will enter the Hamiltonian through a Peierls substitution $\boldsymbol{k} \to \boldsymbol{k} + \frac{e}{\hbar}\boldsymbol{A}$, which is analogous to the replacement of momentum with canonical momentum $\boldsymbol{p} \to \boldsymbol{p} + e\boldsymbol{A}$. The result is $q_\pm \to q_x \pm i(q_y + \frac{e}{\hbar}Bx) = \kappa_\pm$.

With this substitution, the Hamiltonian may be written in terms of harmonic oscillator raising and lowering operators. Denoting the harmonic oscillator wave functions by $Q_j(x)$ and acting on the wave function

$$h_{jX}(\boldsymbol{R}) = \frac{1}{\sqrt{L_y}}e^{i\frac{X}{l_B^2}R_y}Q_j(R_x - X), \tag{3}$$

we verify the commutation relation $[\kappa_-, \kappa_+]h_{jX}(\boldsymbol{R}) = \frac{2}{l_B^2}h_{jX}(\boldsymbol{R})$, where $l_B = \sqrt{\frac{\hbar}{eB}}$ is the magnetic length. Hence, $\kappa_\pm$ satisfies $\kappa_+ = \frac{\sqrt{2}}{l_B}a^+$, $\kappa_- = \frac{\sqrt{2}}{l_B}a$. In particular, if we define the basis states

$$|TjX\rangle = \sum_{\boldsymbol{R}} h_{jX}(\boldsymbol{R})|T\boldsymbol{R}\rangle, \tag{4}$$

where $h_{jX}(\boldsymbol{R})$ is an envelope on the $p_z$ orbitals $|T\boldsymbol{R}\rangle$, then they satisfy $a^+|TjX\rangle = \sqrt{j+1}|T(j+1)X\rangle$ and $a|TjX\rangle = \sqrt{j}|T(j-1)X\rangle$. Note that the index $j$ would be the Landau level index in simpler systems. However, our Hamiltonian below mixes these states $|TjX\rangle$, so that its eigenstates are superpositions of them. These eigenstates are the Landau levels of our system.

Letting $C_\mu = \frac{3a_{\mathrm{CC}}}{\sqrt{2}l_B}t_\mu$, then, we have for example in valley $\xi = +$ the LL Hamiltonian

$$H_+ = \begin{bmatrix} 2\varepsilon + \frac{\Delta}{2} & -Ca & -C_4a^+ & t_\perp \\ -Ca^+ & \frac{\Delta}{2} & -C_3a & -C_4a^+ \\ -C_4a & -C_3a^+ & -\frac{\Delta}{2} & -Ca \\ t_\perp & -C_4a & -Ca^+ & 2\varepsilon - \frac{\Delta}{2} \end{bmatrix}. \tag{5}$$

The Hamiltonian $H_-$ for the other valley $\xi = -$ is obtained by replacing $a$ and $a^+$ with $-a^+$ and $-a$, respectively, in the same basis. The full noninteracting Hamiltonian (both spatial and spin parts) is then

$$\hat{H}_{\mathrm{NI}} = \left(\tfrac{1}{2}\left(1 + \lambda_z^v\right)\hat{H}_+ + \tfrac{1}{2}\left(1 - \lambda_z^v\right)\hat{H}_-\right) - \mu_B B\lambda_z^s, \tag{6}$$

where $\lambda_z^v = \mathbf{1}^o \otimes \sigma_z^v \otimes \mathbf{1}^s$ and $\lambda_z^s = \mathbf{1}^o \otimes \mathbf{1}^v \otimes \sigma_z^s$, in which $\sigma_z^v$ and $\sigma_z^s$ are Pauli matrices acting on the valley and spin spaces $\{+, -\}$ and $\{\uparrow, \downarrow\}$ respectively, and $\mu_B$ is the Bohr magneton.

This Hamiltonian contains three experimental parameters. The magnetic field enters through $B$ and $l_B$, and the electric field enters through the interlayer bias $\Delta$. Pressure enters more subtly through the TB parameters, which were obtained by Munoz *et al.* [17, Table II] by fitting the band structure of the TB model to the band structure calculated by density functional theory (DFT). Another parameter taken from DFT is the layer separation $d$ [17, Table I] which will be important when considering interactions.

To diagonalize $H_\xi$, which contains operators as represented in Eq. (5), we express it as a matrix of scalars by taking matrix elements in a truncated basis of oscillator states

$$\langle TjX|H_\xi|T'j'X\rangle\,, \qquad \begin{array}{l} T, T' = A1, B1, A2, B2, \\ j, j' = 0, 1, 2, \ldots, j_{\max}. \end{array} \tag{7}$$

The coefficients of the wave functions for the states near the neutrality point decrease as $j$ increases. For all magnetic fields and pressures considered here, and for the Landau levels near the neutrality point which we are interested in, the absolute values of the coefficients are smaller than 0.01 when $j > 15$. Therefore, we truncate our expansion at $j_{\max} = 15$.

As a result of the diagonalization, we obtain the Landau levels of the system labeled by the Landau level index or orbital quantum number $n$, with wave functions given by

$$|n\xi\sigma X\rangle = \sum_{Tj} c_{n\xi}^{Tj}|TjX\rangle \times |\sigma\rangle \tag{8}$$

when spin is included. Of the possible values for $n$, two Landau levels $n = 0, 1$ are near the neutrality point. The eight combinations of three binary indices $n = 0, 1$, $\xi = +, -$, $\sigma = \uparrow, \downarrow$ give the eight nearly degenerate low-energy Landau levels (LLLs). Each LLL is highly degenerate because its energy does not depend on the guiding center $X$.

At zero bias, there is a useful symmetry between the valleys which is a consequence of the relation between the Hamiltonians $H_+$ and $H_-$ described in Eq. (5). As a result, their eigenvectors are related by the signed permutation

$$c_{n-}^{Tj} = (-1)^j c_{n+}^{\pi_T j}, \qquad \begin{bmatrix} T \\ \pi_T \end{bmatrix} = \begin{bmatrix} A1 & B1 & A2 & B2 \\ B2 & A2 & B1 & A1 \end{bmatrix}, \tag{9}$$

so that the valley $-$ states have the same spatial distribution as the valley $+$ states but in the opposite layer and lattice sites. (This symmetry identifies $\xi = +$ with the upper layer and $\xi = -$ with the lower layer, which known as the valley-layer correspondence.) Furthermore, their energies are degenerate and may be labeled $E_n$ independently of valley. Over the range of high magnetic fields that we are interested in, bias has negligible effect on coefficients, so the symmetry may be treated as exact and bias can be addressed as a perturbation to the energy. Defining the layer polarization of the LLL $n$ by

$$\Pi_n = \left(\sum_{j=0}^{\infty}\sum_{T_{2D}}\left|c_{n+}^{T_{2D}1j}\right|^2\right) - \left(\sum_{j=0}^{\infty}\sum_{T_{2D}}\left|c_{n+}^{T_{2D}2j}\right|^2\right) \tag{10}$$

and using the symmetry between the valleys, the full noninteracting energy is

$$E_{n\xi\sigma} = E_n - \xi\Pi_n\frac{\Delta}{2} - \sigma\mu_B B. \tag{11}$$

Energies $E_{n\xi\sigma}$ versus bias, and orbital gap $E_1 - E_0$, layer polarization $\Pi_n$, and eigenvector coefficients $c_{n\xi}^{Tj}$ versus magnetic field and pressure, are illustrated in Sec. S1 of the Supplemental Material [18]. Note that when we refer to orbital gap, we mean the splitting caused strictly by noninteracting orbital dynamics, not the energy gap between two LLLs of different orbital, which in general also depends on bias, magnetic field, and interactions.

### B. Coulomb interaction

The Coulomb interaction

$$\hat{V} = \frac{1}{2}\int d^2\boldsymbol{r}\int dz\int d^2\boldsymbol{r}'\int dz'\,\psi^+(\boldsymbol{r}, z)\psi^+(\boldsymbol{r}', z')V(\boldsymbol{r} - \boldsymbol{r}', z, z')\psi(\boldsymbol{r}', z')\psi(\boldsymbol{r}, z) \tag{12}$$

is treated in the Hartree-Fock (HF) approximation, similarly to previous works [6,9–15,19,20]. Throughout this work, we use $\boldsymbol{r}$ for the 2D in-plane position vector, and retain $z$ dependence to address the effects of layer separation, gating, and the spatial extent of the $p_z$ orbitals.

Expanding the Coulomb interaction as its Fourier transform in the in-plane direction as $V(\boldsymbol{r}, z, z') = \sum_{\boldsymbol{q}} e^{i\boldsymbol{q}\cdot\boldsymbol{r}}V(q, z, z')$, and expanding the field operators in the LLL basis,

$$\psi(\boldsymbol{r}, z) = \sum_{n\xi\sigma X}\phi_{n\xi\sigma X}(\boldsymbol{r}, z)c_{n\xi\sigma X} = \sum_{n\xi\sigma X}\left(\sum_{T\boldsymbol{R}} c_{n\xi X}^{T}(\boldsymbol{R})\langle\boldsymbol{r}, z|T\boldsymbol{R}\rangle \times |\sigma\rangle\right)c_{n\xi\sigma X}, \tag{13}$$

we have

$$\hat{V} = \frac{1}{2} \sum_{\substack{n_j \xi_j \sigma_j X_j \\ j=1,2,3,4}} \sum_{\boldsymbol{q}} \bigg[ \int dz \int dz' V(q, z, z') \bigg( \int d^2\boldsymbol{r}\, e^{i\boldsymbol{q}\cdot\boldsymbol{r}} \phi^*_{n_1\xi_1\sigma_1X_1}(\boldsymbol{r}, z) \phi_{n_4\xi_4\sigma_4X_4}(\boldsymbol{r}, z) \bigg)$$

$$\times \bigg( \int d^2\boldsymbol{r}' e^{-i\boldsymbol{q}\cdot\boldsymbol{r}'} \phi^*_{n_2\xi_2\sigma_2X_2}(\boldsymbol{r}', z') \phi_{n_3\xi_3\sigma_3X_3}(\boldsymbol{r}', z') \bigg) \bigg] c^+_{n_1\xi_1\sigma_1X_1} c^+_{n_2\xi_2\sigma_2X_2} c_{n_3\xi_3\sigma_3X_3} c_{n_4\xi_4\sigma_4X_4}. \tag{14}$$

To incorporate both layer separation and the screening effect of metallic double gates used in recent experiments [1–3], we use a propagator of the Coulomb interaction corresponding to equipotential walls at ±$D$. The Fourier transform of this propagator is

$$V(q, z, z') = \frac{2\pi}{A} \frac{e^2}{4\pi\epsilon_r\epsilon_0} \frac{1}{q} \frac{\cosh q(2D - |z' - z|) - \cosh q(z + z')}{\sinh 2qD}, \tag{15}$$

where $D = 20$ nm [1,2] is the distance from the center of the bilayer to the gates above and below, and $\epsilon_r = 6.9$ [21]. Because recent experiments use hexagonal boron nitride as a substrate and dielectric, we have taken the effective dielectric constant to be the dielectric constant of hexagonal boron nitride. Throughout the remainder of this work, the normalization and energy scale will be rewritten as $\frac{2\pi}{A}\frac{e^2}{4\pi\epsilon_r\epsilon_0}\frac{1}{q} = \frac{1}{N_\Phi}\alpha\frac{1}{ql_B}$, where $N_\Phi$ is the number of flux quanta penetrating the bilayer and hence the degeneracy of the system, and $\alpha = \frac{e^2}{4\pi\epsilon_r\epsilon_0 l_B}$ is the interaction energy scale. We include both gating and layer separation because both affect wave-vector scales relevant the LLs, as illustrated in Fig. 2. As mentioned previously, the pressure-dependent layer separation $d$ was obtained by Munoz *et al.* [17, Table I] using DFT.

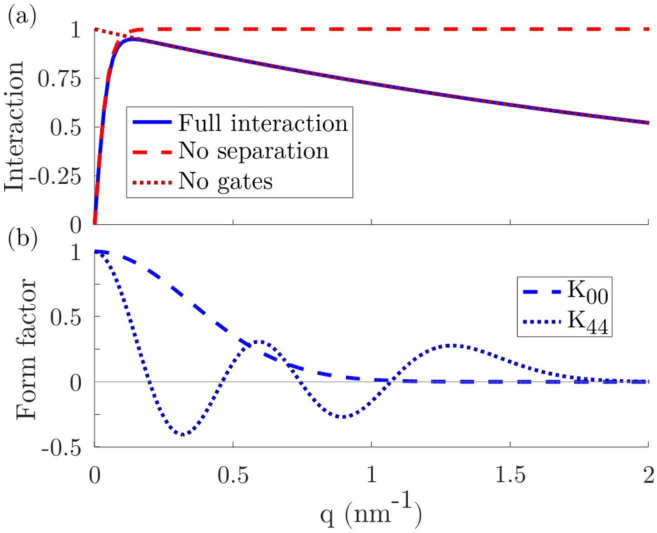

FIG. 2. (a) The interaction strength given by Eq. (19) versus wave vector is plotted here, in units of $\frac{1}{N_\Phi}\alpha\frac{1}{ql_B}$. We use the interlayer case $T_z \neq T_z'$ for demonstration. It can be seen that gating weakens the long-range (small $q$) interactions and layer separation weakens the short-range (large $q$). The dashed curve corresponds to the interaction neglecting separation $d_{\text{eff}}^{T_zT_z'} = 0$, and the dotted curve corresponds to the absence of gates $D \to \infty$. (b) The amplitude of the elementary form factors, as defined in Eq. (22), is plotted versus wave vector on the same scale. As the form factors are integrated against the interaction in the exchange integral of Eq. (29), in this figure we can see that both length scales are relevant in the reciprocal-space support of the wave functions.

Using $d \ll D$, this propagator can be very well approximated as

$$V\left(q, +\frac{d}{2}, -\frac{d}{2}\right) \approx \frac{1}{N_\Phi}\alpha\frac{1}{ql_B}\tanh(qD)e^{-qd}. \tag{16}$$

Taking $D \to \infty$ yields the propagator of Refs. [9–13], while taking $d = 0$ yields the propagator of Ref. [1].

The tight-binding orbitals extend out of the planes of the graphene layers, spreading out charge in the $z$ direction with density

$$P(z) = \int d^2\boldsymbol{r} |\psi_{2p_z}(\boldsymbol{r}, z)|^2, \tag{17a}$$

$$\psi_{2p_z}(r, z) = \left(\frac{Z}{a_0}\right)^{\frac{5}{2}} \frac{1}{\sqrt{32\pi}} z e^{-\frac{Z}{2a_0}\sqrt{r^2+z^2}}, \tag{17b}$$

where $Z = 3.1358$ is the Clementi-Raimondi effective nuclear charge [22] and $a_0$ is the Bohr radius. In previous work, this out-of-plane spatial extent of the $p_z$ orbitals was neglected, i.e., the $z$-direction density was taken to be $P(z) = \delta(z)$ [1,9–13]. This density is integrated out to obtain the layer-resolved Coulomb interaction

$$V_{T_zT_z'}(q) = \int dz \int dz' V(q, z, z') \times P\left(z + (-1)^{T_z}\frac{d}{2}\right) P\left(z + (-1)^{T_z'}\frac{d}{2}\right). \tag{18}$$

We find that this integral can be well approximated by

$$V_{T_zT_z'}(q) = \frac{1}{N_\Phi}\alpha\frac{1}{ql_B}\tanh(qD)e^{-qd_{\text{eff}}^{T_zT_z'}} \tag{19}$$

which has the form of Eq. (16) but uses an effective layer separation $d_{\text{eff}}^{T_zT_z'}$ in place of the physical layer separation $d$. This expression is a fit to exact evaluations of Eq. (18). A complete derivation of these expressions may be found in Sec. S2 of the Supplemental Material [18], together with Fig. S3 which illustrates the validity of the fit given by Eq (19). In the limit $P(z) \to \delta(z)$, the effective interlayer separation becomes the actual layer separation so that the effective intralayer separation vanishes, $d_{\text{eff}}^{T_zT_z'} = d(1 - \delta_{T_zT_z'})$, and we have $V_{11}(q) \to V(q, \frac{d}{2}, \frac{d}{2})$ and $V_{12}(q) \to V(q, \frac{d}{2}, -\frac{d}{2})$. By symmetry, $V_{11}(q) = V_{22}(q)$ and $V_{12}(q) = V_{21}(q)$.

Returning now to Eq. (14), it remains to calculate the Fourier transforms of the wave-function overlaps, or form factors. These are evaluated as

$$\int d^2\boldsymbol{r}\, e^{i\boldsymbol{q}\cdot\boldsymbol{r}}\phi^*_{n_1\xi_1\sigma X_1}(\boldsymbol{r},z)\phi_{n_4\xi_4\sigma X_4}(\boldsymbol{r},z) = \delta_{X_4,X_1-q_y l_B^2} e^{i\frac{q_x}{2}(X_1+X_4)}\sum_{T_z} P\left(z+(-1)^{T_z}\frac{d}{2}\right)J^{T_z}_{\substack{n_1\xi_1\\n_4\xi_4}}(\boldsymbol{q}) \tag{20}$$

with the layer-projected form factors (writing $c^{T_{2D}T_z j}_{n\xi}$ in place of $c^{Tj}_{n\xi}$)

$$J^{T_z}_{\substack{n_1\xi_1\\n_4\xi_4}}(\boldsymbol{q}) = \sum_{j_1 j_4} K_{j_1 j_4}(\boldsymbol{q})\sum_{T_{2D}} c^{T_{2D}T_z j_1\,*}_{n_1\xi_1} c^{T_{2D}T_z j_4}_{n_4\xi_4} \tag{21}$$

and elementary form factors

$$K_{j_1 j_4}(\boldsymbol{q}) = \int dx\, e^{iq_x x} Q_{j_1}\left(x-\frac{q_y l_B^2}{2}\right)Q_{j_4}\left(x+\frac{q_y l_B^2}{2}\right). \tag{22}$$

Each of these expressions is derived in detail in Sec. S2 as well, and a general expression for the elementary form factors follows in Sec. S4, in the Supplemental Material [18]. We will approximate $J^{T_z}_{\substack{n_1\xi_1\\n_4\xi_4}}(\boldsymbol{q}) = J^{T_z}_{\substack{n_1\xi_1\\n_4\xi_1}}(\boldsymbol{q})\delta_{\xi_1\xi_4}$ in the following because the $\xi = +$ and $-$ LLLs have very little overlap. We have broken the full form factors into the layer-projected form factors $J^{T_z}_{\substack{n_1\xi_1\\n_4\xi_4}}(\boldsymbol{q})$ because each LL wave function has support on both layers. This splitting between layers is important because it delocalizes charge and weakens interactions.

The Coulomb interaction is now expressed as

$$\hat{V} = \frac{1}{2}\sum_{\substack{n_j X_j\\ j=1,2,3,4}}\sum_{\xi\xi'\sigma\sigma'}\sum_{\boldsymbol{q}}\sum_{T_z T_{z'}} c^+_{n_1\xi\sigma X_1}c^+_{n_2\xi'\sigma' X_2}c_{n_3\xi'\sigma' X_3}c_{n_4\xi\sigma X_4} \times V_{T_z T_z'}(\boldsymbol{q})\left(\delta_{X_4,X_1-q_y l_B^2}e^{i\frac{q_x}{2}(X_1+X_4)}J^{T_z}_{\substack{n_1\xi\\n_4\xi}}(\boldsymbol{q})\right) \times\left(\delta_{X_3,X_2-q_y l_B^2}e^{i\frac{q_x}{2}(X_2+X_3)}J^{T_z'}_{\substack{n_2\xi'\\n_3\xi'}}(-\boldsymbol{q})\right). \tag{23}$$

In the Hartree-Fock approximation, we replace

$$\tfrac{1}{2}c^+_{n_1\xi_1\sigma_1X_1}c^+_{n_2\xi_2\sigma_2X_2}c_{n_3\xi_3\sigma_3X_3}c_{n_4\xi_4\sigma_4X_4} \to \langle c^+_{n_1\xi_1\sigma_1X_1}c_{n_4\xi_4\sigma_4X_4}\rangle c^+_{n_2\xi_2\sigma_2X_2}c_{n_3\xi_3\sigma_3X_3} - \langle c^+_{n_1\xi_1\sigma_1X_1}c_{n_3\xi_3\sigma_3X_3}\rangle c^+_{n_2\xi_2\sigma_2X_2}c_{n_4\xi_4\sigma_4X_4}, \tag{24a}$$

$$\hat{V}\to\hat{V}_{\rm D}-\hat{V}_{\rm X}, \tag{24b}$$

where $\hat{V}_{\rm D}$ is the direct term and $\hat{V}_{\rm X}$ is the exchange term. We then define the density operators

$$\rho^{\xi\xi'\sigma\sigma'}_{nn'}(\boldsymbol{q}) = \frac{1}{N_\Phi}\sum_{XX'}\delta_{X',X-q_y l_B^2}e^{i\frac{q_x}{2}(X+X')}c^+_{n\xi\sigma X}c_{n'\xi'\sigma' X'} \tag{25}$$

which give a natural basis for studying the system and interactions. In terms of the density operators, the direct term is written as

$$\hat{V}_{\rm D} = N_\Phi\sum_{\boldsymbol{q}}\sum_{\substack{n_1n_2n_3n_4\\ \xi\xi'\sigma\sigma'}} H^{\xi\xi'}_{n_1n_2n_3n_4}(\boldsymbol{q})\langle\rho^{\xi\xi\sigma\sigma}_{n_1n_2}(\boldsymbol{q})\rangle\rho^{\xi'\xi'\sigma'\sigma'}_{n_3n_4}(-\boldsymbol{q}), \tag{26}$$

$$H^{\xi\xi'}_{n_1n_2n_3n_4}(\boldsymbol{q}) = N_\Phi\sum_{T_zT_{z'}}V_{T_zT_z'}(\boldsymbol{q})J^{T_z}_{\substack{n_1\xi\\n_2\xi}}(\boldsymbol{q})J^{T_z'}_{\substack{n_3\xi'\\n_4\xi'}}(-\boldsymbol{q}), \tag{27}$$

and the exchange term is written as

$$\hat{V}_{\rm X} = N_\Phi\sum_{\boldsymbol{q}}\sum_{\substack{n_1n_2n_3n_4\\ \xi\xi'\sigma\sigma'}} X^{\xi\xi'}_{n_1n_4n_3n_2}(\boldsymbol{q})\langle\rho^{\xi\xi'\sigma\sigma'}_{n_1n_2}(\boldsymbol{q})\rangle\rho^{\xi'\xi\sigma'\sigma}_{n_3n_4}(-\boldsymbol{q}), \tag{28}$$

$$X^{\xi\xi'}_{n_1n_4n_3n_2}(\boldsymbol{q}) = \sum_{T_zT_{z'}}\int\frac{d^2\boldsymbol{p}\,l_B^2}{2\pi}H^{\xi\xi'}_{n_1n_4n_3n_2}(\boldsymbol{q})e^{i\boldsymbol{q}l_B\times\boldsymbol{p}l_B}. \tag{29}$$

Since the exchange integral has the symmetries $X^{\xi\xi'}_{klmn}(\boldsymbol{q}) = X^{\xi'\xi}_{klmn}(\boldsymbol{q})$ and $X^{++}_{klmn}(\boldsymbol{q}) = X^{--}_{klmn}(\boldsymbol{q})$, we can write all exchange integrals in terms of the two $X^{++}_{klmn}(\boldsymbol{q})$ and $X^{+-}_{klmn}(\boldsymbol{q})$. Further information on the properties and calculation of the exchange integrals is given in Sec. S4 in the Supplemental Material [18].

We will focus only on spatially uniform solutions and find the lowest-energy state in this subspace. This can be later compared with possible states that break translational symmetry. In other words, we assume $\langle\rho^{\xi\xi\sigma\sigma}_{n_1n_2}(\boldsymbol{q})\rangle = 0$ if $\boldsymbol{q}\neq 0$. [After making this assumption we will generally drop the argument (0), e.g., write $X_{n_1n_4n_3n_2}$ instead of $X_{n_1n_4n_3n_2}(0)$.]

The direct term in the Coulomb interaction is a Coulomb blockade that penalizes layer polarization. In the present case of uniform states, it takes the form of a capacitive correction, as noted in previous work [1,9,11–13]. We find that, up to a constant for fixed total filling $\nu$,

$$\hat{V}_{\rm D} = -N_\Phi\Delta V\sum_{n\xi\sigma}\left(\nu_2\frac{1+\xi\Pi_n}{2}+\nu_1\frac{1-\xi\Pi_n}{2}\right)\rho^{\xi\xi\sigma\sigma}_{nn}, \tag{30}$$

where we have defined the upper- and lower-layer occupations by

$$\nu_{T_z} = \frac{1}{2}\left(\tilde{\nu}-(-1)^{T_z}\sum_{n\xi\sigma}\langle\rho^{\xi\xi\sigma\sigma}_{nn}\rangle\xi\Pi_n\right), \tag{31}$$

with $\tilde{\nu} = \nu + 4$ being the number of filled LLLs, and

$$\Delta V = \frac{\alpha}{l_B}\int dz\int dz'\left(|z'-z+d|-|z'-z|-\frac{d(2z+d)}{2D}\right) \times P(z)P(z'). \tag{32}$$

Hereafter, we will frequently refer to this simply as the Coulomb blockade. In the limits $P(z)\to\delta(z)$, $D\to\infty$ this reproduces the result of previous work, $\Delta V = \alpha\frac{d}{l_B}$ [1,9–13]. Hence, $\Delta V$ can also be written in terms of an effective layer separation $d^{\rm CB}_{\rm eff}$ defined by $\Delta V = \alpha\frac{d^{\rm CB}_{\rm eff}}{l_B}$, and we find that the extent of the $p_z$ orbitals weakens the Coulomb blockade: $d^{\rm CB}_{\rm eff} < d$. This is shown in Fig. S3, and the derivation of these equations from the direct term is given in Sec. S3, in the Supplemental Material [18].

As pointed out by Shizuya [23], exchange interactions with the "Dirac sea" of occupied LLs lower the energy of the $n = 1$ orbitals relative to $n = 0$:

$$\hat{V}_{\rm DS} = \tfrac{1}{2}N_\Phi(X^{++}_{1111}-X^{++}_{0000})\tfrac{1}{2}(1-\lambda^o_z), \tag{33}$$

where $\lambda_z^o = \sigma_z^o \otimes \mathbf{1}^v \otimes \mathbf{1}^s$ in which $\sigma_z^o$ is a Pauli matrix acting on the orbital space $\{0, 1\}$. This exactly compensates for the difference in exchange energy for fully occupied $n = 0$ LLLs compared to $n = 1$. Reference [23] also indicates that the direct interaction with the Dirac sea screens the bias. Because rescaling bias exclusively affects the valley gap, it does not change the balance between any energy scales in a way that would change which ground states appear as a function of magnetic field and bias. Hence, we do not address the direct DS interaction, though it could be relevant for quantitative results in future studies. Adding this "Lamb-type shift" $\Delta_{\text{Lamb}} = \frac{1}{2}(X^{++}_{1111} - X^{++}_{0000})$ to the noninteracting Hamiltonian, we have

$$\hat{H}_{\text{NI+DS}} = N_\Phi \sum_{n\xi\sigma} (E_{n\xi\sigma} + \Delta_{\text{Lamb}}\delta_{1n})\rho^{\xi\xi\sigma\sigma}_{nn}. \qquad (34)$$

The full HF Hamiltonian is then

$$\hat{H}_{\text{HF}} = \hat{H}_{\text{NI+DS}} + \hat{V}_{\text{D}} - \hat{V}_{\text{X}}. \qquad (35)$$

The Hamiltonian matrix element $(H_{\text{HF}})_{(n\xi\sigma),(n'\xi'\sigma')}$ is the coefficient of the density operator $\rho^{\xi\xi'\sigma\sigma'}_{nn'}$. Because the Hamiltonian for a spatially uniform system is block diagonal in $X$, with eight-dimensional blocks indexed by $n\xi\sigma$, the HF problem is reduced to an $8 \times 8$. If the filling factor is $\nu$, then $\tilde{\nu} = \nu + 4$ LLLs are filled, so the many-body eigenstate is

$$|\Psi\rangle = \prod_X \left[ \prod_{j=1}^{\tilde{\nu}} \left( \sum_{n\xi\sigma} A^j_{n\xi\sigma} c^+_{n\xi\sigma X} \right) \right] |\varnothing\rangle, \qquad (36)$$

where $A^j_{n\xi\sigma}$ are the coefficients of the $j$th eigenvector of the matrix $(H_{\text{HF}})_{(n\xi\sigma),(n'\xi'\sigma')}$, ordered by energy with the lowest first. The density matrix elements are given by

$$\langle \rho^{\xi\xi'\sigma\sigma'}_{nn'} \rangle = \sum_{j=1}^{\tilde{\nu}} (A^j_{n\xi\sigma})^* A^j_{n'\xi'\sigma'}. \qquad (37)$$

In the self-consistent approach to solving the HF problem, these density matrix elements are then used to generate a new HF Hamiltonian, and the cycle is iterated until a self-consistent solution has been found. When the solution is found, we refer to it as an LLSD (Landau level Slater determinant) or LLC (Landau level coherent) state if it is given by a diagonal or nondiagonal density matrix, respectively. LLC states can be thought of as the result of LLSD states mixing via coherent superpositions.

It is very useful to calculate the average energy per particle as well. If there are $N_e$ electrons in the LLLs, then since $\tilde{\nu} = \frac{N_e}{N_\Phi}$, up to a constant we have

$$\frac{E_{\text{HF}}}{N_e} = \frac{1}{\tilde{\nu}} \Bigg[ \sum_{n\xi\sigma} \left( E_{n\xi\sigma} + \frac{1}{2}(X^{++}_{1111} - X^{++}_{0000})\delta_{1n} \right) \langle \rho^{\xi\xi\sigma\sigma}_{nn} \rangle - \Delta V \nu_1 \nu_2 - \frac{1}{2} \sum_{\substack{n_1 n_2 n_3 n_4 \\ \xi\xi'\sigma\sigma'}} X^{\xi\xi'}_{n_1 n_4 n_3 n_2} \langle \rho^{\xi\xi'\sigma\sigma'}_{n_1 n_2} \rangle \langle \rho^{\xi'\xi\sigma'\sigma}_{n_3 n_4} \rangle \Bigg]. \qquad (38)$$

This is the energy that the correct many-body solution will minimize. $E_{n\xi\sigma}$ is the noninteracting energy given by Eq. (11), $\frac{1}{2}(X^{++}_{1111} - X^{++}_{0000})$ is the Lamb-type shift [23], $\Delta V$ is the Coulomb blockade given by Eq. (32), and $X^{\xi\xi'}_{n_1 n_4 n_3 n_2}$ are the exchange matrix elements appearing in Eq. (29). By comparing the energies of LLSD states and mixing them into LLC states near their crossings, we can also minimize energy as a function of the parameter or parameters that describe the LLC state's superposition. This method allows us to find the ground state analytically, and is the approach we use in this work.

## III. RESULTS

### A. Phase diagrams

Using the HF calculations presented above, we obtain the ground state for different values of magnetic field, bias, and pressure. For fixed pressure, we draw this as a phase diagram whose different regions represent characteristic ground states as a function of magnetic field and bias. The diagrams evolve continuously with pressure, and we give results for zero pressure, an intermediate pressure of 29.8 GPa, and a high pressure of 96.4 GPa. These were chosen as the minimum and maximum pressures given by Munoz *et al.* [17], plus an intermediate pressure at which all states are easily visible. Since pressure changes the scale of the bias versus magnetic field phase diagrams but does not change their topology, in the following discussion we will use the intermediate pressure case at 29.8 GPa to illustrate.

For low magnetic field and bias, the ground state is the fully spin-polarized (FSP) state, which is layer unpolarized and is drawn in blue in Fig. 3. Further information on this state, and all others, is given in Sec. III B, and they are represented pictorially in Fig. 3(e). As the bias is increased while the magnetic field is kept low, the FSP state is replaced by the fully valley-polarized (FVP) state, which is fully layer polarized and drawn in red. This phase transition occurs when the bias is strong enough to overcome the Coulomb blockade energy. The situation described here can be seen by following the first line cut at $B = 17$ T in Fig. 3(b). To give a more complete picture of the evolution of the ground state with bias, these states' energies and those of higher-energy LLSD states are plotted along in Fig. 4(a) along the same line cut.

The transition from the layer-unpolarized FSP state to the layer-polarized FVP state is an example of a more general trend: as bias increases and overcomes the Coulomb blockade, states with lower-layer polarization are replaced by states with higher-layer polarization, Indeed, in Fig. 4, the slope of energy versus bias for each LLSD state is the total layer polarization $\sum_{n\xi\sigma} \xi \Pi_n \langle \rho^{\xi\xi\sigma\sigma}_{nn} \rangle$. Because the energy of the fully layer-polarized FVP state decreases most steeply with bias, it is always the ground state at sufficiently high bias. Conversely, the energy of the layer-unpolarized FSP state is unaffected by bias. This pattern persists throughout the phase diagram for all magnetic fields. Consider increasing the magnetic field to $B = 28$ T, shown by the second line cut in Fig. 3(b) and by Fig. 4(b). At this field the transition between the FSP and FVP states no longer occurs directly but has an intermediate state, which is known as the partially orbitally polarized (POP) state and is drawn in orange. This state is partially polarized

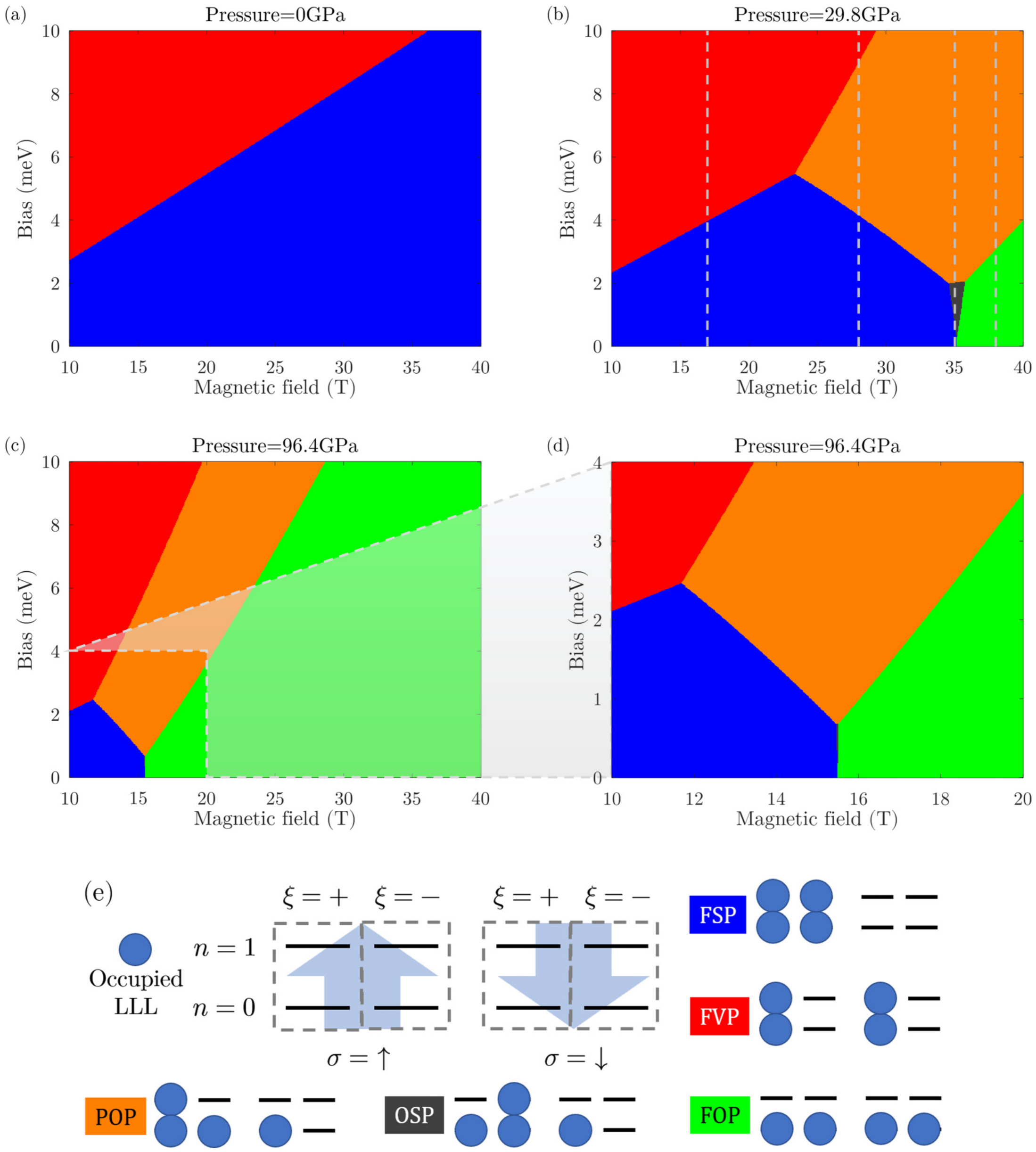

FIG. 3. Phase diagrams for (a) zero, (b) intermediate, and (c) high pressures are given; (d) magnifies (c). Five LLSD and no LLC states appear. Notice that applied pressure literally compresses the phase diagram so that all transitions occur at progressively lower fields, as explained in the text, but that the overall topology remains unchanged. The dashed lines on P = 29.8 GPa correspond to the traces in Fig. 4. (e) A schematic of the dot-diagram depiction of states devised by Lambert and Côté [11,12], and the dot-diagram representation of the different states appearing in our phase diagrams.

in all three degrees of freedom; in particular, it is partially valley and hence partially layer polarized. In this way the trend continues: as bias overcomes the Coulomb blockade, each successive ground state has greater layer polarization.

The transition to the POP state is driven by a transition in energy scale dominance that occurs as the magnetic field is increased, much like the transition between bias and the Coulomb blockade energy which happened as the bias was increased. This transition occurs as the orbital gap $E_1 - E_0$, which scales as $B$, overcomes the exchange energy, which scales as $\sqrt{B}$. This transition induces the general trend of spin and valley polarization being traded for orbital polarization as the magnetic field increases. This trend follows from the more precise rule that exchange favors states with same-spin, same-valley pairs of LLs occupied, which can be read from Fig. 3(e) as pairs of vertically aligned dots. These pairs are favorable because only states of the same spin and valley have nonzero overlap, so that their energy is reduced by exchange.

As the magnetic field is increased further, the trend of orbital polarization becoming favored over spin and valley polarization as the magnetic field is increased brings into the phase diagram two additional orbitally polarized states not previously observed. At $B = 35$ T, shown by the third line cut in the phase diagram of Fig. 3(b) and by the energy of the states in Fig. 4(c), the low-bias ground state is the orbitally and spin-polarized (OSP) state, drawn in charcoal. It

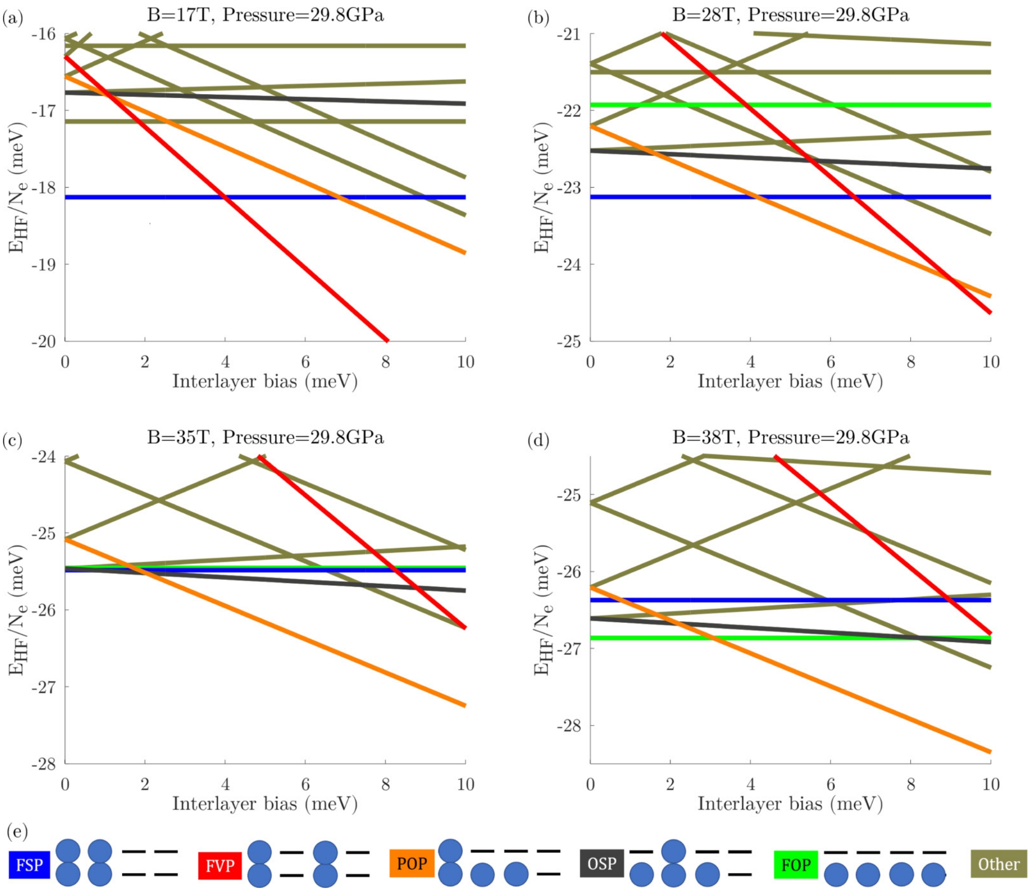

FIG. 4. (a)–(d) The state energies are plotted here as a function of bias for the representative magnetic field line cuts in Fig. 3(b). Pressure is fixed at P = 29.8 GPa because it does not change the topology of the phase diagram. (e) The diagrams of Fig. 3(e), which give the colors used to label the ground states, are repeated here for convenience. The energies of higher-energy LLSD states are plotted in olive to demonstrate the presence of these states and their energies relative to the ground states.

is partially orbitally and spin polarized, but valley unpolarized and hence minimally layer polarized, so that it replaces the FSP state as the bottom rung of the ladder of increasingly layer-polarized states. At $B = 38$ T, shown by the fourth line cut in Fig. 3(b) and by Fig. 4(d), the fully orbitally polarized (FOP) state, drawn in green, likewise replaces the OSP state as the minimally layer-polarized ground state at low bias. The FOP state is fully orbitally polarized and has no valley or spin polarization, so it is layer unpolarized.

Now that we understand the energy scales driving the phase transitions in Fig. 3(b), it is straightforward to understand the changes in the phase diagram with pressure. As pressure increases, the orbital gap increases more steeply with magnetic field (see Fig. S1 in the Supplemental Material [18]) so that the transitions to orbitally polarized states occur at lower magnetic fields. Likewise, pressure decreases layer separation and thus weakens the Coulomb blockade so that transitions to layer-polarized states also occur at slightly lower bias. Hence, pressure literally compresses the phase diagram into a smaller region in the space of magnetic field and bias. In Fig. 3(a), the orbitally polarized states are not visible in the phase diagram simply because the orbital gap does not grow quickly enough at zero pressure for these states to appear at an experimentally reasonable magnetic field. In principle, the previously unobserved OSP and FOP states could also have been predicted by previous zero-pressure models, but would have required magnetic fields above those theoretically explored thus far. In particular, the POP, OSP, and FOP states would have appeared in Fig. 3(a) if the figure were extended to include extraordinarily high magnetic fields.

Pressure drastically narrows the part of the phase diagram occupied by the OSP state, as can be seen by comparing Fig. 3(b) to Figs. 3(c) and 3(d). This is best explained through Fig. 4, in which we see that for any magnetic field, the OSP state's energy is between the FSP and FOP states' energies at zero bias. However, when the exchange-favored FSP and orbital-gap-favored FOP states' energies are nearly equal in Fig. 4(c), the OSP state becomes the ground state for a small range of bias due to the small slope of its energy with bias, i.e., its small but nonzero layer polarization. Hence, the range of magnetic fields over which the OSP state is the ground state is dictated by the relative energies of the bias, the exchange interaction, the orbital gap. As pressure is increased, the growth of the orbital gap with magnetic field also increases, so that the orbital gap outweighs the bias and the OSP state is replaced by the FOP state at a lower magnetic field.

By increasing the layer polarization of the $n = 1$ orbital, as shown in Fig. S1(d) of the Supplemental Material [18], pressure also reduces the total layer polarization $\sum_{n\xi\sigma} \xi \Pi_n \langle \rho_{nn}^{\xi\xi\sigma\sigma} \rangle$ of the OSP state, while increasing the total layer polarization of the POP and FVP states. As a result, at elevated pressures the POP state replaces the OSP state at a lower bias. This effect of increasing total layer polarization is also responsible for steepening the slopes of the boundary between the FVP and POP states and the boundary between the POP and FOP states when comparing Figs. 3(b) and 3(c).

The five LLSD states we have presented are all possible states that may appear in our model even at arbitrary magnetic field, bias, and pressure. This is clear because increasing pressure beyond 96.4 GPa or the magnetic field beyond 40 T will simply further stabilize the FOP state, and increasing bias beyond 10 meV further stabilizes the FVP state, and the partially orbitally and layer-polarized POP state will always intermediate between them. It is interesting that no LLC states manifest as ground states in our results because one would generally expect the interaction to mix LLSD states when they are close in energy, namely, at the phase boundaries in Fig. 3 or the energy crossings in Fig. 4. This finding contrasts with previous results [11–13,15], and we explain this discrepancy in Sec. III C.

### B. State configurations and descriptions

Of the five LLSD states we find in the phase diagram, three (the FSP, FVP, and FOP states) are fully polarized in one degree of freedom while unpolarized in the other, and two (the POP and OSP states) have mixed partial polarization. We give their wave functions and brief characterizations below.

#### *1. Fully spin-polarized (FSP) state*

The FSP state is polarized only in spin and is written as

$$|\Psi_{\text{FSP}}\rangle = \prod_X (c^+_{0+\uparrow X} c^+_{0-\uparrow X} c^+_{1+\uparrow X} c^+_{1-\uparrow X})|\varnothing\rangle. \tag{39}$$

This state has no layer polarization and two same-spin, same-valley pairs. It is maximally favored by the Zeeman splitting, Coulomb blockade, and exchange interaction, so that it appears at low magnetic field and bias. Many previous studies [1,6,11–13,15] have also found this state.

#### *2. Fully valley-polarized (FVP) state*

The FVP state is polarized only in valley and is written as

$$|\Psi_{\text{FVP}}\rangle = \prod_X (c^+_{0+\uparrow X} c^+_{0+\downarrow X} c^+_{1+\uparrow X} c^+_{1+\downarrow X})|\varnothing\rangle. \tag{40}$$

This state has maximal layer polarization and two same-spin, same-valley pairs. It is maximally favored by the bias and exchange interaction, so that it is found at high bias and low magnetic field. Many previous studies [1,6,11–13,15] have also found this state.

#### *3. Fully orbitally polarized (FOP) state*

The FOP state is polarized only in orbital and is written as

$$|\Psi_{\text{FOP}}\rangle = \prod_X (c^+_{0+\uparrow X} c^+_{0+\downarrow X} c^+_{0-\uparrow X} c^+_{0-\downarrow X})|\varnothing\rangle. \tag{41}$$

This state has no layer polarization and no same-spin, same-valley pairs. It is maximally favored by the Coulomb blockade and orbital gap, so that it appears at low bias and high magnetic field. This state has not appeared in any previous studies because it requires a large orbital gap to manifest.

#### *4. Partially orbitally polarized (POP) state*

The POP state is partially polarized in all three indices, with 3-to-1 ratios of $n = 0$ to 1, $\xi = +$ to $-$, and $\sigma = \uparrow$ to $\downarrow$, and is written as

$$|\Psi_{\text{POP}}\rangle = \prod_X (c^+_{0+\uparrow X} c^+_{0+\downarrow X} c^+_{0-\uparrow X} c^+_{1+\uparrow X})|\varnothing\rangle. \tag{42}$$

This state has partial layer polarization and one same-spin, same-valley pair. It is partially favored by the bias, Zeeman splitting, Coulomb blockade, exchange interaction, and orbital gap, so that it appears at intermediate bias and magnetic field. It has been predicted and observed before [1,2,15].

#### *5. Orbitally and spin-polarized (OSP) state*

The OSP state is partially polarized in orbital and spin, but is unpolarized in valley, and is written as

$$|\Psi_{\text{OSP}}\rangle = \prod_X (c^+_{0+\uparrow X} c^+_{0+\downarrow X} c^+_{0-\uparrow X} c^+_{1-\uparrow X})|\varnothing\rangle. \tag{43}$$

This state has very small layer polarization and one same-spin, same-valley pair. (Layer polarization is nonzero due to unequal polarizations of the orbitals, $\Pi_0 \neq \Pi_1$.) It is partially favored by the Zeeman splitting, exchange interaction, and orbital gap, and maximally favored by the Coulomb blockade, so that it appears at low bias and intermediate magnetic field. It has neither been predicted nor observed in previous studies.

### C. Absence of LLC states

The five states we observe are all LLSD states, despite the presence of interactions which in general mix the noninteracting eigenstates into LLC states. To explain the absence of LLC states, we focus on a particular example which has appeared in previous work [11–13,15], the FSP-FVP state. This state continuously interpolates between the eponymous LLSD states with two spin-valley superpositions, and can be parametrized by two angles $\theta_0, \theta_1$ as

$$|\Psi_{\text{FSP-FVP}}\rangle = \prod_X [c^+_{0+\uparrow X}(\cos\theta_0 c^+_{0-\uparrow X} + \sin\theta_0 c^+_{0+\downarrow X}) c^+_{1+\uparrow X}(\cos\theta_1 c^+_{1-\uparrow X} + \sin\theta_1 c^+_{1+\downarrow X})]|\varnothing\rangle. \tag{44}$$

For this state not to appear at the phase boundary between the FSP and FVP states, it must be energetically unfavorable. We can verify this analytically by calculating the concavity of its energy, given in Eq. (S32) in the Supplemental Material [18], with respect to the superposition parameters. To simplify this, we describe the superposition using a single parameter with the common [13,15] approximation $\theta_0 = \theta_1 \equiv \theta$. This approximation, that the transitions occur in tandem, is good because exchange couples the $n = 0$ occupation to the $n = 1$ occupation. (Only same-spin, same-valley pairs lower the energy of the state by exchange, so it is beneficial for the $n = 0$ and 1 superpositions to transfer from $-\uparrow$ to $+\downarrow$ together.) In this case, the concavity of the energy with respect to the − ↑ LLL occupation is

$$\left(\frac{d}{d\ \cos^2\theta}\right)^2 \nu \frac{E_{\mathrm{HF}}^{\text{FSP-FVP}}}{N_e} = 2\Delta V(\Pi_0+\Pi_1)^2 + 2\alpha\big[\big(X_{0000}^{+-}+2X_{0110}^{+-}+X_{1111}^{+-}\big)-\big(X_{0000}^{++}+2X_{0110}^{++}+X_{1111}^{++}\big)\big]. \tag{45}$$

If this expression is negative, then the superposition is unfavorable and the energy is minimized at end points $\cos^2\theta = 1$ or 0, i.e., the FSP or FVP LLSD states. We find that it is negative for all magnetic fields and pressures in our model.

There are two contributions to the concavity in Eq. (45): the Coulomb blockade ($\Delta V$) term, which is always $\geqslant 0$, and the exchange ($X_{klmn}^{\xi\xi'}$) term, which is always $\leqslant 0$. Each exchange integral $X_{klmn}^{\xi\xi'}$ is positive, so the exchange term actually has a positive intervalley $+X_{klmn}^{+-}$ and negative intravalley $-X_{klmn}^{++}$ component. Recalling the valley-layer correspondence, however, the intervalley integrals are always smaller because the layer separation $d$ weakens interlayer interactions.

From this we see that the FSP-FVP LLC state will be unfavorable if the Coulomb blockade is too weak, or if the disparity between the intravalley and intervalley exchange integrals is too large. In our model, the spatial extent of the $p_z$ orbitals weakens the Coulomb blockade, and the layer-resolved form factors derived from exact diagonalization increase the intravalley-intervalley disparity. In contrast, if the extent of the $p_z$ orbitals is neglected and the valley-layer correspondence is assumed to be exact, then the FSP-FVP state appears as in previous work using similar interaction propagators [11–13].

We further compare the effects of the spatial extent of the $p_z$ orbitals, layer separation, gating, and layer-resolved form factors in Sec. III D to explain their impacts on the model. We find that the layer-resolved exact diagonalization form factors are principally responsible for the absence of superpositions. Determining whether superpositions are favorable using energy concavity extends similarly to other pairs of LLSD states, and we use this method to confirm that no other LLC states appear in our model. We give the concavities of the relevant superpositions in Sec. S5 and discuss the physical interpretation of each term in Sec. S6 in the Supplemental Material [18].

### D. Effects of 3D $p_z$ orbitals, layer separation, gating, form factors, and heterostructures

Our model includes the spatial extent of the $p_z$ orbitals, layer separation, metallic gates, and layer-resolved form factors found by exact diagonalization. Since previous models have included some of these effects while neglecting others, it is worthwhile to explore their respective impacts on the phase diagram. To this end, in Fig. 5 we plot phase diagrams in which we have either neglected only one of these effects, or included only one and neglected the others. These phase diagrams are meant to be compared with our main result in Fig. 3(b) and with one another. We choose to compare at P = 29.8 GPa, where the differences are most visible. In the

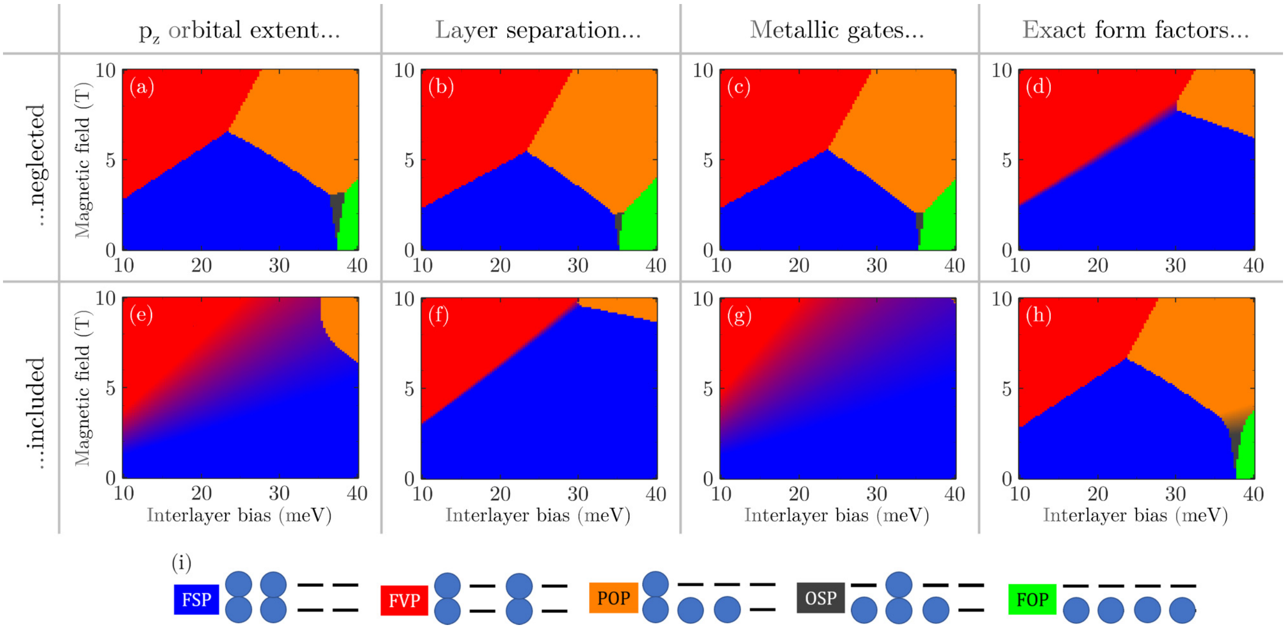

FIG. 5. These phase diagrams, calculated for P = 29.8 GPa, show what our model would predict if, in Coulomb interaction calculations, we (a) neglected the spatial extent of the $p_z$ orbitals by taking $P(z) \to \delta(z)$, (b) neglected layer separation by taking $d = 0$, (c) neglected metallic gates by taking $D \to \infty$, (d) neglected exact diagonalization form factors by using one-component wave functions with $c_{n+}^{Tj} = \delta_{T,B1}\delta_{j,n}$, or (e)–(h) include only one of the aforementioned effects while neglecting the others. (i) The diagrams and colors used to label the LLSD states are repeated here. As the LLC states continuously interpolate between LLSD states, the LLC states are colored by interpolating between the colors of the LLSD states they mix.

following, we will proceed column by column through Fig. 5 to explore each effect in turn.

The spatial extent of the $p_z$ orbitals is the focus of Figs. 5(a) and 5(e); it in general weakens the Coulomb interaction, as it spreads the electron density out vertically. We can see this effect by comparing Fig. 5(a), where it is neglected, to Fig. 3(b) and Figs. 5(b) and 5(c), where it is included. When it is neglected, the FSP state extends to higher magnetic field because the $p_z$ orbitals' extent weakens exchange (which favors the FSP state over orbitally polarized states) and to higher bias because the $p_z$ orbitals' extent weakens the Coulomb blockade (which favors the FSP state over the FVP state). The OSP state extends to higher bias as well in Fig. 5(a) for the same reason regarding the Coulomb blockade. Indeed, the effective layer separations plotted in Fig. S3 in the Supplemental Material [18] also show that the $p_z$ orbitals' extent weakens both the Coulomb blockade and exchange interactions. The weakening of the Coulomb blockade is also apparent in Fig. 5(e), where the partially layer-polarized POP state appears at lower biases than in Figs. 5(f) and 5(g).

Layer separation is the focus of Figs. 5(b) and 5(f). Layer separation greatly decreases the intervalley exchange integrals. These are the off-diagonal matrix elements in the Hamiltonian that mix LLLs of different valleys, producing avoided crossings that we see these as LLC states. Therefore, neglecting $d$ narrows the FSP-FVP LLC state substantially in Fig. 5(f) as compared to Figs. 5(e) and 5(g). In Fig. 5(b), this effect is not apparent because the LLC state does not appear. However, layer separation also reduces the intravalley exchange integrals by a small amount. These integrals are responsible for stabilizing spin- and valley-polarized states; therefore, the exchange-favored FSP state extends to slightly higher magnetic field in Fig. 5(b), where layer separation is neglected, than in Fig. 3(b), where it is included.

The metallic gates are the focus of Figs. 5(c) and 5(g). Being separated from the bilayer by a large distance $D = 20$ nm in our model, the gates have the smallest impact on the phase diagram out of all the effects we consider. They slightly screen both the Coulomb blockade and the exchange interaction, so that without the gates, the FSP and FVP states in Fig. 5(c) take up a slightly larger region of phase space than with the gates in Fig. 3(b). The region of the phase diagram occupied by orbitally polarized states is smallest in Fig. 5(g) out of all the lower row figures, illustrating that the gates weaken the exchange interaction less than any of the other effects.

The layer-resolved exact diagonalization form factors are the focus of Figs. 5(d) and 5(h); they physically describe the spatial distribution of the LL wave functions [cf. Eq. (8) and the coefficients plotted in Fig. S2 the Supplemental Material [18]] split between the two layers, have the most substantial impacts on the phase diagram. They not only weaken interactions more than any other effect, but also render superpositions unfavorable. Weakening the Coulomb blockade brings phase transitions to lower bias and weakening exchange interaction brings phase transitions to lower magnetic fields, so that the phase diagram is scaled down. This is seen when comparing Fig. 5(d) to the other upper row figures [5(a)–5(c)], and when comparing Fig. 5(h) to the other lower row figures [5(e)–5(g)]. The suppression of superpositions is evinced by the facts that Fig. 5(d) is the only upper row figure to feature the FSP-FVP LLC state, and that Fig. 5(h) is the only lower row figure which does *not* feature the aforementioned LLC state.

Figure 5(h) is also notably the only diagram to feature the OSP-POP state, a superposition between the OSP and POP states. It has constant partial orbital and spin polarization and continuously evolving partial valley polarization, and is given by

$$|\Psi_{\text{OSP-POP}}\rangle = \prod_X [c^+_{0+\uparrow X} c^+_{0+\downarrow X} c^+_{0-\uparrow X} (\cos\theta\, c^+_{1+\uparrow X} + \sin\theta\, c^+_{1-\uparrow X})]|\varnothing\rangle. \tag{46}$$

Further information on this state is in Sec. S5 in the Supplemental Material [18].

We have examined here only a representative subset of the possible combinations of included and neglected parameters. Our model is also compatible with previous models by changing the parameters described above, plus a few constants. For example, we have reproduced the onset and end of the FSP-FVP state given by Ref. [11] by removing gates and the spatial extent of the $p_z$ orbitals, using simplified form factors, neglecting the Lamb-type shift, and using the TB parameters and dielectric constant given therein; and we have reproduced the LLL energy levels of Ref. [19] by using the same approximations and additionally setting the orbital gap to 0. Additionally, to facilitate comparison of Fig. 5 to previous theoretical work, in producing these phase diagrams we have taken $d = 0$ only in the Coulomb interaction propagator and keep $d \neq 0$ in the Coulomb blockade as in Ref. [1], and use $c^{Tj}_{n+} = \delta_{T,B1}\delta_{j,n}$ only in the Coulomb interaction calculations but not in $E_{n\xi\sigma}$, as in Refs. [9–13].

A modification of the Coulomb interaction we have not addressed in our model is that of screening by more complex heterostructures than a uniform boron nitride dielectric. Recently, the experiment of Chuang *et al.* [4] on stacked BLG and WSe$_2$ monolayers or bilayers showed that WSe$_2$ brings the appearance of the POP state to lower magnetic fields, and noted that thin dielectric layers primarily screen short-range interactions, which weakens exchange. Weakening exchange disfavors the FSP and FVP states, so that the POP state appears at a lower magnetic field.

## IV. CONCLUSION

We have produced Landau level phase diagrams of charge-neutral ($\nu = 0$) BLG as a function of magnetic field, bias, and pressure. We found noninteracting eigenstates and energies using a four-band tight-binding model with hoppings between each pair of lattice sites. Projecting into the eight LLLs near the Fermi level and treating the Coulomb interaction through the Hartree-Fock approximation, we studied how gate screening, layer separation, the spatial extent of the $p_z$ orbitals, and layer-resolved form factors found by exact diagonalization impact the interaction and phase diagrams. All parameters were determined by *ab initio* calculations [17,22] or independent experimental measurements [21].

Five LLSD states (FSP, FVP, POP, OSP, and FOP) manifest as ground states. Two of these (OSP and FOP) previously have been neither theoretically predicted to appear nor observed experimentally. The appearance of the orbitally polarized states (POP, OSP, and FOP) is driven by noninteracting dynamics overtaking the Coulomb interaction as the dominant energy scale, and this transition is controlled by pressure and the magnetic field. The absence of LLC states in our results, in comparison to similar theoretical work using parameter-free long-range Coulomb propagators [9–13], is unique to our model. We isolated the use of exact diagonalization form factors which respect the inequivalence between valley and layer as the source of this change. This emphasizes that, due to the small energy scales involved in this system, even parameters or effects which appear small may in fact be significant.

We chose to focus on $\nu = 0$, but our model may readily be applied for other filling factors. Likewise, we focused on ground-state phase diagrams, but our model can also be used to calculate excited-state energies and single-particle energy gaps to explain transport or cyclotron resonance experiments, as in Ref. [11] or [19], respectively, for example. These are natural followup topics for us to explore in future work, alongside the effects of correlations and fluctuations, and the possibilities of nonuniform states.

Comparison to experiment is subtle. Conduction modes have been proposed for both discontinuous and continuous transitions: conduction domain walls percolating through the bulk for discontinuous transitions between LLSD states [24,25] and gapless edge excitations for continuous transitions through LLC states [26,27]. Furthermore, due to the confining potential of the edge, the ground state in the bulk may deform into a different ordered state near the edge, which could obscure measurements of the bulk [26,28]. With these caveats, we believe it is reasonable to interpret the experimentally detected transitions and reflecting transitions in the bulk ground state, with some uncertainty due to masking by edge states. Recent experiments [1,2] found a single transition at low magnetic fields, the FSP-to-FVP transition, bifurcating into two transitions, the FSP-to-POP and POP-to-FVP transitions, at $B = 12$ T at zero pressure. The signature (e.g., conductivity spike) of the FVP-to-FSP transition is similar to that of the transitions involving the POP state, which is consistent with our finding that all transitions are of the same order, i.e., all are discontinuous. Our phase diagrams also share with experiment the same topology of the single transition bifurcating as the magnetic field is increased; however, in our model the POP state can only be brought down to experimentally accessible magnetic fields with pressure. This suggests opportunities for both theoretical and experimental research. Theoretically, our model appears to be missing a key ingredient that helps stabilize orbitally polarized states. Experimentally, this would mean that the orbitally polarized states we predict, the OSP and FOP states, are likely to be accessible at lower magnetic fields than we present here.

Comparing Refs. [11,13] and this work, which did not find the POP state around $B = 12$ T at zero pressure, with Refs. [1,15], which did, suggests some missing ingredients. For example, LL mixing provides screening [1,11,29–31] and, together with the electron-phonon interaction, can induce symmetry-breaking interactions [6,14,15] which may stabilize the POP state. These symmetry-breaking interactions stabilize a canted antiferromagnetic state [6,15,20], which does not appear in our model but is supported by experimental evidence [3,7]. Additionally, one experiment by Li *et al.* [3] using a different device geometry and tilted magnetic field found a metallic state between the FSP and FVP states. We have not addressed these characteristics in our model, and at this point the nature of the metallic state remains an open question as well.

Even small or weak effects may be important due to the small energy scale of the LLLs. This is demonstrated by the above comparison of published results; by our comparison of the effects of model details in Sec. III D, particularly the nature of the form factors; and by a comparison of the orbital gap plotted in Fig. S1 in the Supplemental Material [18] to the phase diagrams in Fig. 3, which shows the significant impact of increasing orbital splitting by only a few meV/T. We are working to understand the aforementioned effects in a physically transparent way. Such understanding will be necessary to answer the many remaining open questions for research in this field and to explore its continually expanding possibilities, both theoretical and experimental.

## ACKNOWLEDGMENTS

This material is based upon work supported by the National Science Foundation Graduate Research Fellowship Program under Grant No. DGE1255832. Any opinions, findings, and conclusions or recommendations expressed in this material are those of the author and do not necessarily reflect the views of the National Science Foundation. B.G. acknowledges training provided by the Computational Materials Education and Training (CoMET) NSF Research Traineeship (Grant No. DGE-1449785).

---

[1] B. M. Hunt, J. I. A. Li, A. A. Zibrov, L. Wang, T. Taniguchi, K. Watanabe, J. Hone, C. R. Dean, M. Zaletel, R. C. Ashoori, and A. F. Young, Nat. Commun. **8**, 948 (2017).
[2] J. Li, Y. Tupikov, K. Watanabe, T. Taniguchi, and J. Zhu, Phys. Rev. Lett. **120**, 047701 (2018).
[3] J. Li, H. Fu, Z. Yin, K. Watanabe, T. Taniguchi, and J. Zhu, Phys. Rev. Lett. **122**, 097701 (2019).
[4] Y.-W. Chuang, J. Li, H. Fu, K. Watanabe, T. Taniguchi, and J. Zhu, Phys. Rev. B **100**, 195402 (2019).
[5] R. T. Weitz, M. T. Allen, B. E. Feldman, J. Martin, and A. Yacoby, Science **330**, 812 (2010).
[6] M. Kharitonov, Phys. Rev. Lett. **109**, 046803 (2012).
[7] P. Maher, C. R. Dean, A. F. Young, T. Taniguchi, K. Watanabe, K. L. Shepard, J. Hone, and P. Kim, Nat. Phys. **9**, 154 (2013).
[8] E. McCann and M. Koshino, Rep. Prog. Phys. **76**, 056503 (2013).
[9] R. Côté, J. Lambert, Y. Barlas, and A. H. MacDonald, Phys. Rev. B **82**, 035445 (2010).
[10] R. Côté, J. P. Fouquet, and W. Luo, Phys. Rev. B **84**, 235301 (2011).
[11] J. Lambert and R. Côté, Phys. Rev. B **87**, 115415 (2013).

[12] J. Lambert, *Ferro-Aimants de Hall Dans La Bicouche de Graphène*, Ph.D. thesis, Université de Sherbrooke, 2013.

[13] A. Knothe and T. Jolicoeur, Phys. Rev. B **94**, 235149 (2016).

[14] M. Kharitonov, Phys. Rev. B **85**, 155439 (2012).

[15] G. Murthy, E. Shimshoni, and H. A. Fertig, Phys. Rev. B **96**, 245125 (2017).

[16] J. Jung and A. H. MacDonald, Phys. Rev. B **89**, 035405 (2014).

[17] F. Munoz, H. P. Ojeda Collado, G. Usaj, J. O. Sofo, and C. A. Balseiro, Phys. Rev. B **93**, 235443 (2016).

[18] See Supplemental Material at http://link.aps.org/supplemental/10.1103/PhysRevB.101.195432 for additional details regarding the derivations and results presented here.

[19] Y. Barlas, R. Côté, K. Nomura, and A. H. MacDonald, Phys. Rev. Lett. **101**, 097601 (2008).

[20] M. Kharitonov, Phys. Rev. B **86**, 075450 (2012).

[21] A. Laturia, M. L. Van de Put, and W. G. Vandenberghe, npj 2D Mater. Appl. **2**, 6 (2018).

[22] E. Clementi and D. L. Raimondi, J. Chem. Phys. **38**, 2686 (1963).

[23] K. Shizuya, Phys. Rev. B **86**, 045431 (2012).

[24] T. Jungwirth and A. H. MacDonald, Phys. Rev. Lett. **87**, 216801 (2001).

[25] K. Dhochak, E. Shimshoni, and E. Berg, Phys. Rev. B **91**, 165107 (2015).

[26] G. Murthy, E. Shimshoni, and H. A. Fertig, Phys. Rev. B **90**, 241410(R) (2014).

[27] G. Murthy, E. Shimshoni, and H. A. Fertig, Phys. Rev. B **93**, 045105 (2016).

[28] A. Knothe and T. Jolicoeur, Phys. Rev. B **92**, 165110 (2015).

[29] R. Nandkishore and L. Levitov, Phys. Rev. Lett. **104**, 156803 (2010).

[30] E. V. Gorbar, V. P. Gusynin, V. A. Miransky, and I. A. Shovkovy, Phys. Rev. B **85**, 235460 (2012).

[31] E. V. Gorbar, V. P. Gusynin, A. B. Kuzmenko, and S. G. Sharapov, Phys. Rev. B **86**, 075414 (2012).